Chemical Science

ROYAL SOCIETY OF CHEMISTRY

EDGE ARTICLE

View Article Online
View Journal | View Issue

Check for updates

Cite this: *Chem. Sci.*, 2023, **14**, 8474

All publication charges for this article have been paid for by the Royal Society of Chemistry

Received 1st April 2023
Accepted 24th July 2023

DOI: 10.1039/d3sc01698f

rsc.li/chemical-science

Restriction of intramolecular rotation for functionalizing metal nanoclusters†

Junsheng Xin,‡[ab] Jing Xu,‡[a] Chen Zhu,[a] Yupeng Tian,[a] Qiong Zhang,*[a] Xi Kang*[ab] and Manzhou Zhu*[ab]

The restriction of intramolecular rotation has been extensively exploited to trigger the property enhancement of nanocluster-based materials. However, such a restriction is induced mainly by intermolecular aggregation. The direct restriction of intramolecular rotation of metal nanoclusters, which could boost their properties at the single molecular level, remains rarely explored. Here, ligand engineering was applied to activate intramolecular interactions at the interface between peripheral ligands and metallic kernels of metal nanoclusters. For the newly reported $Au_4Ag_{13}(SPhCl_2)_9(DPPM)_3$ nanocluster, the molecule-level interactions between the Cl terminals on thiol ligands and the Ag atoms on the cluster kernel remarkably restricted the intramolecular rotation, endowing this robust nanocluster with superior thermal stability, emission intensity, and non-linear optical properties over its cluster analogue. This work presents a novel case of the restriction of intramolecular rotation (*i.e.*, intramolecular interaction-induced property enhancement) for functionalizing metal clusters at the single molecular level.

1 Introduction

Metal nanocluster chemistry remains a thriving research field.[1–6] Metal nanoclusters with atomically precise structures occupy the gap between discrete atoms and plasmonic nanoparticles, revealing the size evolutions and structural transformations of metallic materials in their initial forms.[1,2] Besides, metal clusters or cluster-based nanomaterials display intriguing physicochemical properties that can be rationalized in terms of their discrete electronic states and quantum size effects.[7–16] In addition, such properties (*e.g.*, optical, electrochemical, magnetic, and chiral properties) show a clear relationship with cluster structures, and any perturbations in their compositions/constructions will induce tremendous changes in properties.[17–24] In this context, the atomically precise nature of nanoclusters facilitates structure–property correlation elucidation, making them remarkably useful for the rational customization of cluster-based nanomaterials with tailored performance.[25–34]

Several efficient strategies have been exploited to control the physicochemical properties of metal nanoclusters, such as alloying, ligand engineering, aggregation-induced emission (AIE), cluster-based network construction, *etc.*[35–38] Among them, AIE has been extensively utilized for fabricating strongly emissive cluster-based nanomaterials.[37,39,40] Generally, the energy dissipation of energy-excited nanoclusters encompasses two pathways: (i) radiative transitions mainly through photoluminescence (PL), and (ii) non-radiative transitions that could be affected by intra- or inter-molecular vibrations.[3] It is generally accepted that ordered aggregation would reduce the energy release of energy-excited clusters through non-radiative transitions, and accordingly, energy dissipation through radiative transition (PL) would increase.[3,41] For previously reported cluster cases with the solvent- or the cation-induced AIE performance, the restriction of intermolecular motion was considered the leading cause for triggering the emission enhancement.[42–50] Compared with the intermolecular control, the intramolecular operation is more likely to regulate the electronic structures of cluster molecules, and further boost their properties at the root level.[51] However, the emission enhancement of most cluster cases with the AIE behavior was activated by intermolecular aggregation. The direct restriction of intramolecular rotation of metal nanoclusters, which could boost their properties at the single molecular level, remains rarely explored. The investigation of the restriction of intramolecular rotation-induced emission enhancement in cluster science calls for more effort.

[a]*Department of Chemistry, Centre for Atomic Engineering of Advanced Materials, Key Laboratory of Structure and Functional Regulation of Hybrid Materials of Ministry of Education, Anhui University, Hefei, Anhui 230601, China. E-mail: zhangqiong.314@163.com; kangxi_chem@ahu.edu.cn; zmz@ahu.edu.cn*

[b]*Institutes of Physical Science and Information Technology, Anhui Province Key Laboratory of Chemistry for Inorganic/Organic Hybrid Functionalized Materials, Anhui University, Hefei, Anhui 230601, China*

† Electronic supplementary information (ESI) available: Methods, Fig. S1–S21 and Tables S1–S4. CCDC 2223274. For ESI and crystallographic data in CIF or other electronic format see DOI: https://doi.org/10.1039/d3sc01698f

‡ Junsheng Xin and Jing Xu contributed equally to this work.

Open Access Article. Published on 26 July 2023. Downloaded on 5/4/2026 8:39:30 AM. This article is licensed under a Creative Commons Attribution-NonCommercial 3.0 Unported Licence.

© 2023 The Author(s). Published by the Royal Society of Chemistry

Open Access Article. Published on 26 July 2023. Downloaded on 5/4/2026 8:39:30 AM. This article is licensed under a Creative Commons Attribution-NonCommercial 3.0 Unported Licence.

We previously reported the crystallization-induced emission enhancement (CIEE) of an $Au_4Ag_{13}(SPhMe_2)_9(DPPM)_3$ nanocluster (**Au_4Ag_{13}–SPhMe$_2$** in short; DPPM = bis(diphenylphosphino)methane), and the emission enhancement of this nanocluster in its crystalline state was triggered by the generated intermolecular C–H$\cdots\pi$ interactions.[52] Based on this cluster template, we are motivated to introduce additional intramolecular interactions, which hopefully further boost its properties at the single-molecule level. Herein, ligand engineering has been exploited to produce an $Au_4Ag_{13}(SPhCl_2)_9(DPPM)_3$ nanocluster (**Au_4Ag_{13}–SPhCl$_2$** in short), acting as a structural analogue to **Au_4Ag_{13}–SPhMe$_2$**. The molecule-level interactions between the Cl terminals on thiol ligands and the Ag atoms on the cluster kernel remarkably restricted the intramolecular rotation, endowing the **Au_4Ag_{13}–SPhCl$_2$** nanocluster with superior thermal stability and emission intensity over its analogue, **Au_4Ag_{13}–SPhMe$_2$**, whether in solution, amorphous, or crystalline state. Besides, the **Au_4Ag_{13}–SPhCl$_2$** cluster displayed excellent nonlinear optical properties, and has been utilized as a new type of optical limiter. In this context, the molecule-level Cl$\cdots$Ag interaction-induced restriction of intramolecular rotation has successfully functionalized the metal nanoclusters.

2 Experimental methods

Materials

All chemicals, including silver nitrate ($AgNO_3$, 99.9%, metal basis), tetrachloroauric(III) acid ($HAuCl_4\cdot 3H_2O$, ≥99.99%, metal basis), 2,5-dimethylbenzenethiol ($HSPhMe_2$, ≥99.99%), 2,6-dichlorobenzenethiol ($HSPhCl_2$, ≥99.99%), bis(diphenylphosphino)methane ($Ph_2P–C_2H_5–PPh_2$, DPPM, 98%), sodium borohydride ($NaBH_4$, 99%), methylene chloride (CH_2Cl_2, HPLC grade), methanol (CH_3OH, HPLC grade), and *n*-hexane (Hex, HPLC grade) were purchased from Sigma-Aldrich and used without further purification.

Synthesis of $Au_4Ag_{13}(DPPM)_3(SPhMe_2)_9$

The preparation of $Au_4Ag_{13}(DPPM)_3(SPhMe_2)_9$ was based on the reported method.[52]

Synthesis of $Au_4Ag_{13}(DPPM)_3(SPhCl_2)_9$

The $Au_4Ag_{13}(DPPM)_3(SPhCl_2)_9$ nanocluster was prepared using the same synthetic procedure as that used for $Au_4Ag_{13}(DPPM)_3(SPhMe_2)_9$, while the thiol ligand source was altered to $HSPhCl_2$.

Crystallization of $Au_4Ag_{13}(DPPM)_3(SPhMe_2)_9$ and $Au_4Ag_{13}(DPPM)_3(SPhCl_2)_9$ nanoclusters

The crystallization of the $Au_4Ag_{13}(DPPM)_3(SPhMe_2)_9$ nanocluster was performed based on the reported method. For the $Au_4Ag_{13}(DPPM)_3(SPhCl_2)_9$ nanocluster, single crystals were cultivated at room temperature by diffusing the *n*-hexane (insoluble reagent) into the CH_2Cl_2 solution of the nanocluster in a bottle. After 14 days, black crystals were collected, and the structures of these nanoclusters were determined.

Characterization

All UV-vis optical absorption spectra of nanoclusters dissolved in CH_2Cl_2 were recorded using an Agilent 8453 diode array spectrometer, whose background correction was made using a CH_2Cl_2 blank. Nanocluster samples were dissolved in CH_2Cl_2 to make dilute solutions, followed by spectral measurement (1 cm path length quartz cuvette).

Photoluminescence (PL) spectra were measured on an FL-4500 spectrofluorometer with the same optical density (OD) of ~0.1.

Quantum yields (QYs) were measured with dilute solutions of nanoclusters on a HORIBA FluoroMax-4P.

X-ray photoelectron spectroscopy (XPS) measurements were performed on a Thermo ESCALAB 250 configured with a monochromatized Al Kα (1486.8 eV) 150 W X-ray source, 0.5 mm circular spot size, a flood gun to counter charging effects, and analysis chamber base pressure lower than 1×10^{-9} mbar.

X-ray crystallography

The data collection for single-crystal X-ray diffraction (SC-XRD) of all nanocluster crystal samples was carried out on a Stoe Stadivari diffractometer under nitrogen flow, using graphite-monochromatized Cu Kα radiation (λ = 1.54186 Å). Data reductions and absorption corrections were performed using the SAINT and SADABS programs, respectively. The structure was solved by direct methods and refined with full-matrix least squares on F^2 using the SHELXTL software package. All non-hydrogen atoms were refined anisotropically, and all the hydrogen atoms were set in geometrically calculated positions and refined isotropically using a riding model. All crystal structures were treated with PLATON SQUEEZE, and the diffuse electron densities from these residual solvent molecules were removed. The CCDC number of the $Au_4Ag_{13}(DPPM)_3(SPhCl_2)_9$ nanocluster is 2223274.

3 Results and discussion

The **Au_4Ag_{13}–SPhCl$_2$** nanocluster was prepared using the same synthetic procedure as **Au_4Ag_{13}–SPhMe$_2$**,[52] while the thiol ligand source was altered to $HSPhCl_2$. Single crystals of **Au_4Ag_{13}–SPhCl$_2$** were cultivated by diffusing the *n*-hexane (insoluble reagent) into the CH_2Cl_2 solution of this cluster in a bottle. After 14 days, black crystals were collected, and the structures of these nanoclusters were determined. The experimental Au : Ag ratio of **Au_4Ag_{13}–SPhCl$_2$** was determined to be 24.3% : 75.7% *via* X-ray photoelectron spectroscopy (Fig. S1†), matching well with the theoretical value (23.5% : 76.5%).

The crystal structure of **Au_4Ag_{13}–SPhCl$_2$** was determined by single-crystal X-ray diffraction (Fig. S2 and Table S1†). No counterion was observed in the crystal lattice of **Au_4Ag_{13}–SPhCl$_2$**, demonstrating the electrical neutrality of the cluster molecule. Besides, the compositions of the two nanoclusters were verified by electrospray ionization mass spectrometry and thermogravimetric analysis (ESI-MS and TGA; Fig. S3 and S4†). In this context, the nominal electron count of the **Au_4Ag_{13}–SPhCl$_2$** nanocluster was determined to be 8 (*i.e.*, 17(Au + Ag) −

Open Access Article. Published on 26 July 2023. Downloaded on 5/4/2026 8:39:30 AM. This article is licensed under a Creative Commons Attribution-NonCommercial 3.0 Unported Licence.

9($SPhCl_2$) = 16e), the same as that of **Au_4Ag_{13}–SPhMe$_2$**.[52,53] Besides, the overall configuration of **Au_4Ag_{13}–$SPhCl_2$** was similar to that of **Au_4Ag_{13}–SPhMe$_2$**, demonstrating that the two cluster structural analogues formed an ideal platform for investigating the (i) ligand effect on structures of metal nanoclusters and (ii) structure–property correlations at the atomic level.

Structurally, the overall structure of **Au_4Ag_{13}–$SPhCl_2$** followed a core@shell configuration (Fig. 1), encompassing an icosahedral Au_4Ag_9 core that was enwrapped by three $Ag_1(SPhCl_2)_2(DPPM)_1$ and one $Ag_1(SPhCl_2)_3$ claw-like motif units (Fig. 1A–D). Each thiol ligand bonded with a shell Ag atom and a core Ag atom, while each bidentate phosphine ligand connected a shell Ag atom and a core Au atom. Accordingly, four gold atoms existed in **Au_4Ag_{13}–$SPhCl_2$**, one located in the innermost kernel of the clusters, and the other three situated on the icosahedral kernel, corresponding exactly to the three DPPM ligands (Fig. 1A–C). Besides, the three peripheral $Ag_1(SPhCl_2)_2(DPPM)_1$ motif structures showed axial symmetry along a three-fold axis crossing the innermost Au kernel and the vertex Ag atom from $Ag_1(SPhCl_2)_3$ (Fig. 1E). However, the structural distribution of these $Ag_1(SPhCl_2)_2(DPPM)_1$ substructures was uneven, and the rotation angles were 145.64°, 111.39°, and 99.12° (Fig. 1F). By comparison, the corresponding rotation angles were the same as 119.57° for the **Au_4Ag_{13}–SPhMe$_2$** nanocluster (Fig. S5†). In addition, the Ag–S bond lengths in the $Ag_1(SPhCl_2)_3$ unit followed the same pattern: uneven distribution in **Au_4Ag_{13}–$SPhCl_2$** and even distribution in **Au_4Ag_{13}–SPhMe$_2$** (Fig. S6†). In this context, the structure of **Au_4Ag_{13}–$SPhCl_2$** exhibited a quasi-C_3 axial symmetry, while that of **Au_4Ag_{13}–SPhMe$_2$** was symmetrical along with a C_3 axis. We propose that the quasi-symmetry of the **Au_4Ag_{13}–$SPhCl_2$** nanocluster resulted from the intramolecular Ag–Cl interactions on the nanocluster surface (*vide infra*). Furthermore, we compared the corresponding bond lengths between **Au_4Ag_{13}–$SPhCl_2$** and **Au_4Ag_{13}–SPhMe$_2$** nanoclusters (Fig. S7†). The much longer Au(icosahedral kernel)···M(icosahedral surface), M(icosahedral surface)···M(icosahedral surface), and Ag(icosahedral surface)···S(motif) bond lengths of **Au_4Ag_{13}–$SPhCl_2$** relative to those of **Au_4Ag_{13}–SPhMe$_2$** demonstrated the extended core configuration and the core–shell interfaces of the former nanocluster. Moreover, these two nanoclusters exhibited completely different crystalline unit cell parameters (Fig. S8†), resulting from the ligand effect on the supramolecular chemistry of the two nanoclusters.

For the **Au_4Ag_{13}–SPhMe$_2$** nanocluster, several intermolecular C–H···π interactions were detected, while no intramolecular interaction between peripheral ligands (*i.e.*, carbon tails) and core metals was observed.[52] By comparison, the structure of the **Au_4Ag_{13}–$SPhCl_2$** nanocluster embodied abundant molecular and supramolecular interactions:

(i) At the molecular level, several intramolecular interactions between Cl from thiol ligands and Ag from the cluster core were formed in **Au_4Ag_{13}–$SPhCl_2$** (Fig. 2A), which was absent in **Au_4Ag_{13}–SPhMe$_2$** (Fig. 2B). The distances between Ag and Cl atoms in **Au_4Ag_{13}–$SPhCl_2$** were 2.858, 2.999, and 3.003 Å (on an average, 2.95 Å), which were not only much shorter than the sum of van der Waals radii of Ag and Cl atoms (1.72 Å + 1.80 Å = 3.52 Å), but also longer than the sum of the atomic radii of Ag and Cl atoms (1.44 Å + 1.62 Å = 3.06 Å). Accordingly, the interactions between Ag and Cl atoms in **Au_4Ag_{13}–$SPhCl_2$** could be considered covalent interactions.

(ii) At the supramolecular level, apart from the intermolecular C–H···π interactions, several Cl···H interactions were

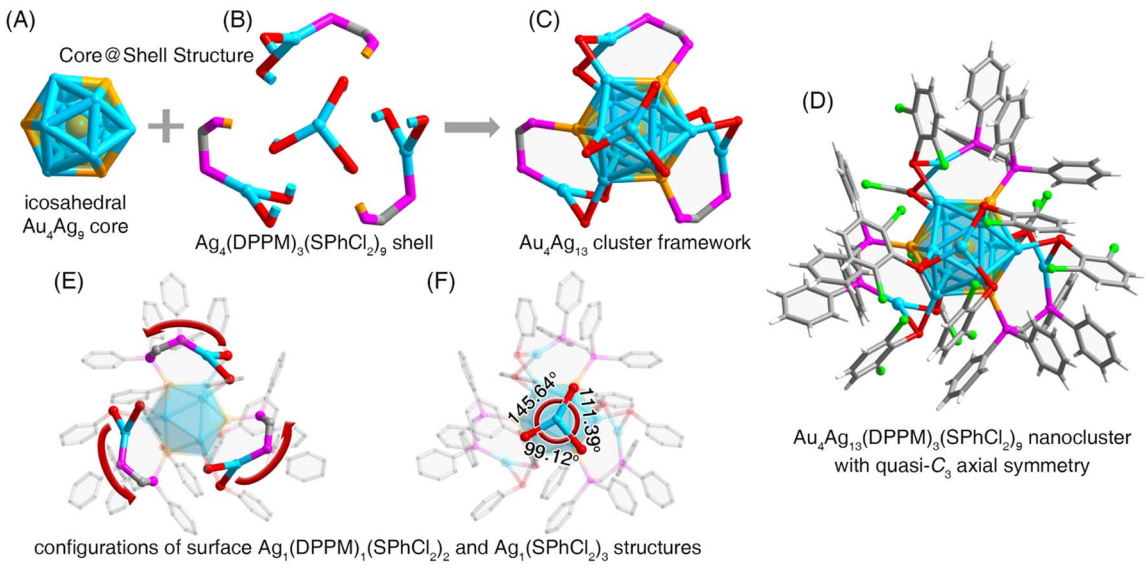

Fig. 1 Structure anatomy of the **Au_4Ag_{13}–$SPhCl_2$** nanocluster. (A) The icosahedral Au_4Ag_9 kernel with an Au_1 kernel@Au_3Ag_9 shell configuration. (B) The $Ag_4(DPPM)_3(SPhCl_2)_9$ shell, involving an $Ag_1(SPhCl_2)_3$ and three $Ag_1(DPPM)_1(SPhCl_2)_2$ surface motif structures. (C) The overall cluster framework of **Au_4Ag_{13}–$SPhCl_2$**. (D) The structure of **Au_4Ag_{13}–$SPhCl_2$** with quasi-C_3 axial symmetry. (E and F) The quasi-triply symmetric configuration of surface $Ag_1(DPPM)_1(SPhCl_2)_2$ and $Ag_1(SPhCl_2)_3$ structures. Color labels: yellow = Au; blue = Ag; red = S; magenta = P; green = Cl; grey = C; white = H.

© 2023 The Author(s). Published by the Royal Society of Chemistry

Open Access Article. Published on 26 July 2023. Downloaded on 5/4/2026 8:39:30 AM.
This article is licensed under a Creative Commons Attribution-NonCommercial 3.0 Unported Licence.

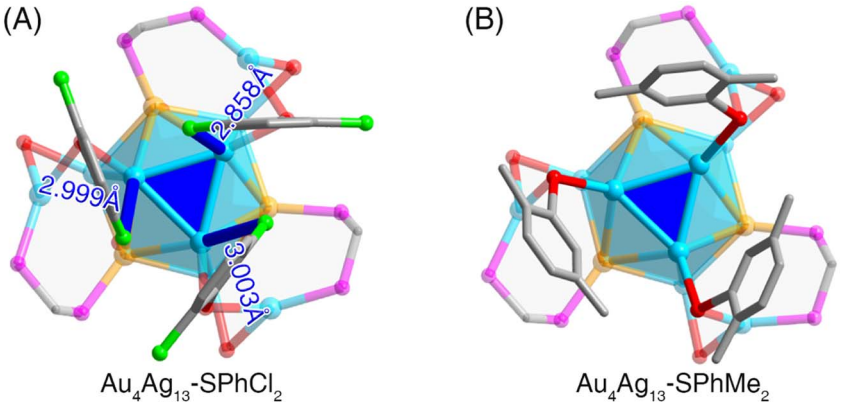

Fig. 2 Structure comparisons between Au_4Ag_{13}–$SPhCl_2$ and Au_4Ag_{13}–$SPhMe_2$ nanoclusters. (A) The presence of Ag···Cl interactions in the Au_4Ag_{13}–$SPhCl_2$ nanocluster. (B) The absence of intramolecular core–shell interactions in the Au_4Ag_{13}–$SPhMe_2$ nanocluster. Color labels: yellow = Au; blue = Ag; red = S; magenta = P; green = Cl; grey = C.

observed in the crystal lattice of **Au_4Ag_{13}–$SPhCl_2$** (Fig. S9†). In this context, the **Au_4Ag_{13}–$SPhCl_2$** nanocluster presented more abundant inter-cluster stabilizing factors relative to **Au_4Ag_{13}–$SPhCl_2$**.

Collectively, such abundant molecular and intramolecular interactions were conducive to making the **Au_4Ag_{13}–$SPhCl_2$** nanocluster more robust and restricting the intramolecular rotation of the overall configuration further.

The abundant molecular and intramolecular interactions would trigger the restriction of intramolecular rotation of the **Au_4Ag_{13}–$SPhCl_2$** cluster framework, hopefully having enormous effects on the physicochemical properties of metal nanoclusters.[54] First, although **Au_4Ag_{13}–$SPhCl_2$** and **Au_4Ag_{13}–$SPhMe_2$** showed the same core@shell geometric configuration, the ligand effect endowed these two nanoclusters with different electronic structures, derived from their comparable optical absorptions. As shown in Fig. S10A,† **Au_4Ag_{13}–$SPhMe_2$** exhibited a broad UV-vis signal at 430 nm, and two shoulder bands at 330 and 260 nm. For comparison, the **Au_4Ag_{13}–$SPhCl_2$** nanocluster showed similar bands at 405, 310, and 270 nm. A 25 nm blue shift was observed for comparing the 405 nm absorption of **Au_4Ag_{13}–$SPhCl_2$** relative to the 430 nm band of **Au_4Ag_{13}–$SPhMe_2$** (Fig. S10A†). Such a blue shift might result from the higher ΔE value (*i.e.*, HOMO–LUMO gap value) of the **Au_4Ag_{13}–$SPhCl_2$** nanocluster relative to **Au_4Ag_{13}–$SPhMe_2$** (*vide infra*), and thus the photoexcited transitions of the former cluster required higher energies, corresponding to shorter absorption wavelengths.

Time-dependent optical absorption spectra of the two Au_4Ag_{13} cluster analogues were monitored for confirming their thermal stability. The characteristic absorption of **Au_4Ag_{13}–$SPhCl_2$** at 405 nm almost remained unchanged within 48 hours (Fig. 3A). By comparison, the characteristic UV-vis signal of **Au_4Ag_{13}–$SPhMe_2$** at 430 nm gradually decreased in intensity after two hours and completely disappeared in approximately six hours, indicating degradation (Fig. 3B). The TGA results suggested that **Au_4Ag_{13}–$SPhMe_2$** started to lose weight at 220 °C, much lower than that of **Au_4Ag_{13}–$SPhCl_2$** (260 °C), demonstrating the enhanced thermal stability of the **Au_4Ag_{13}–$SPhCl_2$** nanocluster (Fig. S4†). The enhanced thermal stability of **Au_4Ag_{13}–$SPhCl_2$** relative to **Au_4Ag_{13}–$SPhMe_2$** was rational by considering that the additional Ag···Cl interactions in **Au_4Ag_{13}–$SPhCl_2$** made its skeleton more robust, and thus the cluster framework would remain intact with time.

The restriction of intramolecular rotation would influence the photoluminescence (PL) of the Au_4Ag_{13} cluster analogues from two aspects: the emission wavelength and the PL intensity. First, the two clusters displayed similar excitation spectra, demonstrating that their excitations came from the same excited states (Fig. S10B†). In addition, the PL spectra of **Au_4Ag_{13}–$SPhCl_2$** occurred at 670 nm in any state, representing a 25 nm blue shift compared to the solution or the crystalline form of **Au_4Ag_{13}–$SPhMe_2$**, or a 40 nm blue shift relative to the amorphous state of **Au_4Ag_{13}–$SPhMe_2$** (Fig. 3C, D and S11†). Such blue shifts corresponded to the difference in optical absorptions of the two nanoclusters, demonstrating their distinctively electronic structures. As for the PL intensity, the crystal of **Au_4Ag_{13}–$SPhMe_2$** exhibited enhanced PL intensity compared to its solutions or amorphous forms, revealing the CIEE phenomenon of this cluster.[52] Such an emission enhancement was also detected for **Au_4Ag_{13}–$SPhCl_2$** whose crystal displayed a high PL quantum yield (QY) of 52.60%, much higher than that of its CH_2Cl_2 solution and amorphous solids with a PL QY of 11.78% and 32.29%, respectively. In addition, **Au_4Ag_{13}–$SPhCl_2$** showed superior emission intensity over its analogue, **Au_4Ag_{13}–$SPhMe_2$**, whether in solution, amorphous, or crystalline state (Fig. S11†). Wu *et al.* have demonstrated that the PL intensity of emissive nanoclusters was parallel with the ligand's capability of donating electrons to the metal core.[55] Here, the –$SPhMe_2$ ligand has a much higher electron donating ability than –$SPhCl_2$, while the PL intensity of **Au_4Ag_{13}–$SPhMe_2$** was much lower. In this context, we propose that such full-scale PL enhancement of **Au_4Ag_{13}–$SPhCl_2$** resulted from the presence of abundant intra-cluster Ag···Cl and inter-cluster Cl···H interactions in **Au_4Ag_{13}–$SPhCl_2$**, which remarkably restrained the vibrations/rotations of cluster molecules at molecular and

Open Access Article. Published on 26 July 2023. Downloaded on 5/4/2026 8:39:30 AM. This article is licensed under a Creative Commons Attribution-NonCommercial 3.0 Unported Licence.

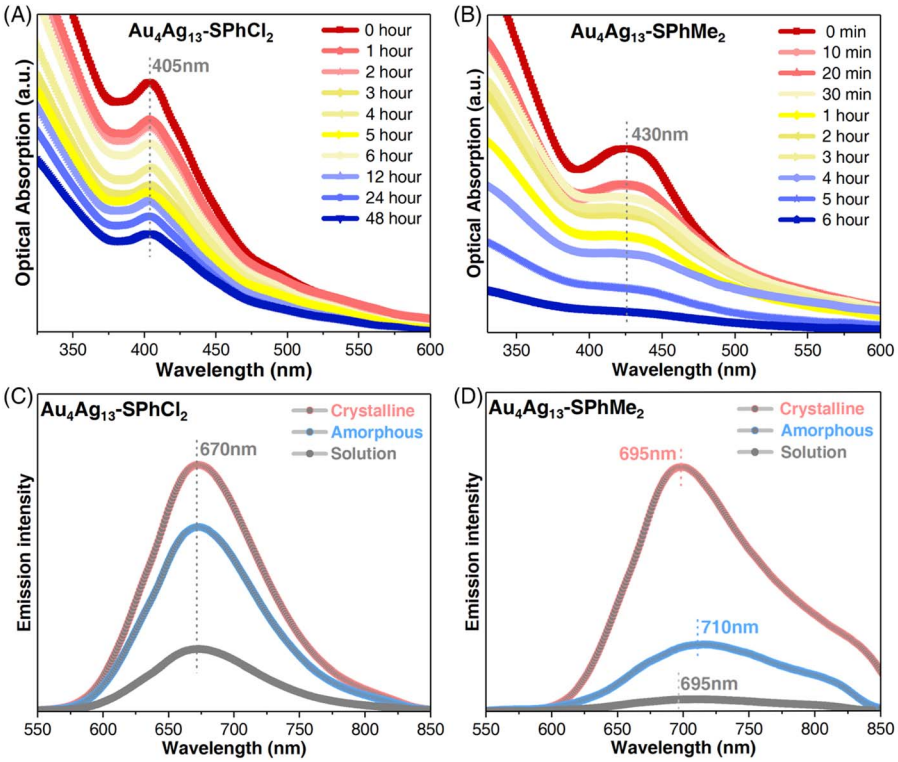

Fig. 3 Property comparisons between Au_4Ag_{13}–$SPhCl_2$ and Au_4Ag_{13}–$SPhMe_2$ nanoclusters. (A) Optical absorption spectra confirming the thermal stability of the Au_4Ag_{13}–$SPhCl_2$ nanocluster over time. (B) Optical absorption spectra confirming the thermal stability of the Au_4Ag_{13}–$SPhMe_2$ nanocluster over time. (C) PL characterizations of Au_4Ag_{13}–$SPhCl_2$ in different states. (D) PL characterizations of Au_4Ag_{13}–$SPhMe_2$ in different states.

supramolecular levels. For example, for the intramolecular rotation aspect, the Ag···Cl interaction-induced inhibited vibrations/rotations might be reflected in several aspects, including the structural vibrations of the kernel–surface interface and the metal–ligand surface structures, and the structural rotations of substituent groups of peripheral ligands. Thus, the energy dissipation of the photo-excited clusters through the radiative transition (*i.e.*, PL) increased.[3] Besides, as shown in Fig. S10C and D,† the fluorescence lifetimes of the **Au_4Ag_{13}–$SPhCl_2$** nanocluster crystal or solution (2.28 or 0.33 μs, respectively) were much longer than those of **Au_4Ag_{13}–$SPhMe_2$** (0.65 and 3.31 ns, respectively).[52] Such a significant difference in fluorescence lifetimes results from their diverse excitation–emission processes, which were proposed to be affected by their different intermolecular and intramolecular interactions.

Theoretical calculations have been carried out to determine the energies of the two nanoclusters (Fig. S12†). The overall structure of the **Au_4Ag_{13}–$SPhCl_2$** nanocluster displayed a much lower energy barrier compared to **Au_4Ag_{13}–$SPhMe_2$** (*i.e.*, −21 110 a.u. *versus* −13 621 a.u.), demonstrating the enhanced stability of **Au_4Ag_{13}–$SPhCl_2$** to a certain extent. Such an enhancement may result from the more robust structure of the **Au_4Ag_{13}–$SPhCl_2$** nanocluster with several intra-cluster Ag···Cl interactions.

Besides, the nonlinear optical (NLO) properties of the two Au_4Ag_{13} cluster analogues were compared. It was found that there was no linear absorption in the wavelength range between 700 and 900 nm for both Au_4Ag_{13} clusters (Fig. 3A), indicating that there was no energy level corresponding to an electron transition in this range. In this context, it is impossible to generate single-photon-excited up-converted fluorescence upon using such excitation wavelengths. If frequency-up converted fluorescence occurred upon excitation with a tunable laser in the range of 1150–2200 nm, it could be safely attributed to the multiphoton excited fluorescence (MPEF).

To thoroughly investigate the NLO properties of these Au_4Ag_{13} clusters, we measured the MPEF spectra of **Au_4Ag_{13}–$SPhCl_2$** in three states, *i.e.*, the crystalline, amorphous, and solution states. By tuning the pump wavelengths incrementally from 1150 to 2200 nm while keeping the input power fixed and then recording the MPEF intensity, the multi-photon fluorescence (2PEF and 3PEF) spectra were detected (Fig. 4A). The multi-photon absorption (MPA) spectra of **Au_4Ag_{13}–$SPhCl_2$** were not presented in the solution state since they showed inconspicuous MPEF intensity among the investigated wavelength range (Fig. 4A, C, S13 and S14†). Besides, the **Au_4Ag_{13}–$SPhMe_2$** cluster in the crystalline state presented a moderate MPEF (2PEF and 3PEF) centered at 640 nm with an optimal excitation wavelength of 1400 nm (Fig. 4B, D, S15 and S16†). In addition, the fluorescence intensity of the 2PEF spectra of **Au_4Ag_{13}–$SPhMe_2$** in the amorphous state was 1.4 times higher than that of **Au_4Ag_{13}–$SPhCl_2$** (Fig. 4E). The maximal two-photon

 © 2023 The Author(s). Published by the Royal Society of Chemistry

Open Access Article. Published on 26 July 2023. Downloaded on 5/4/2026 8:39:30 AM.
This article is licensed under a Creative Commons Attribution-NonCommercial 3.0 Unported Licence.

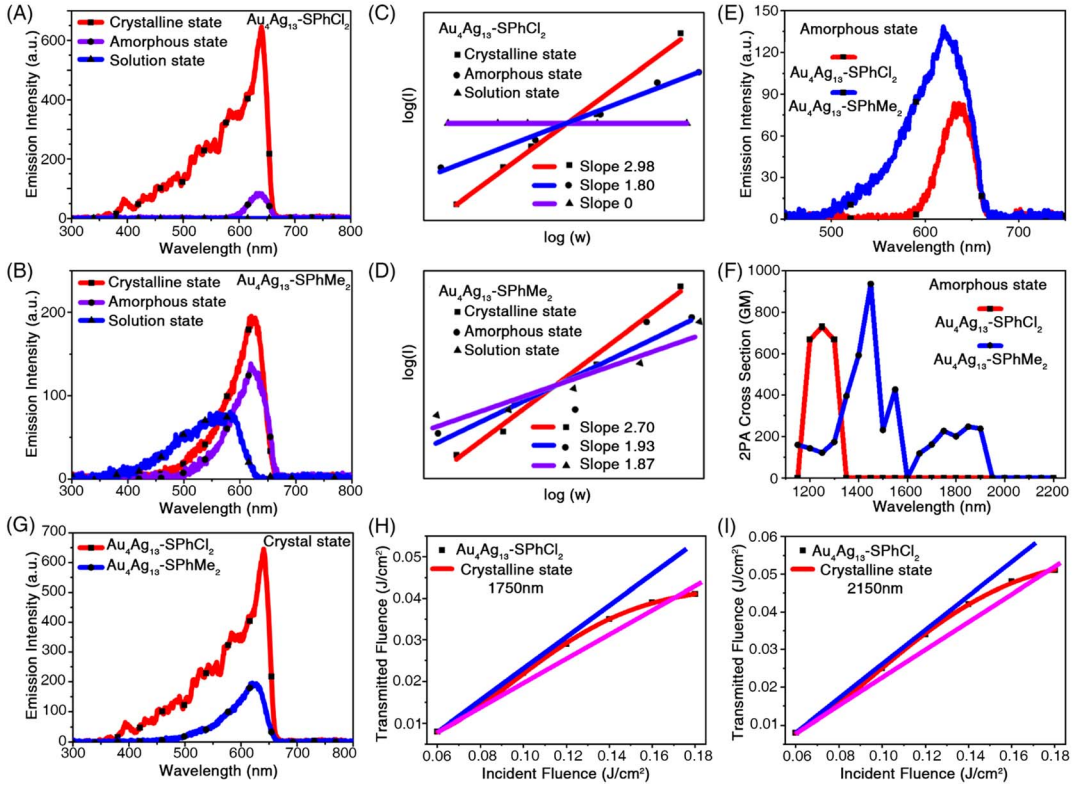

Fig. 4 Non-linear optical properties of Au_4Ag_{13}–$SPhCl_2$ and Au_4Ag_{13}–$SPhMe_2$ nanoclusters. (A) 2PEF and 3PEF spectra of Au_4Ag_{13}–$SPhCl_2$ in crystalline (1450 nm), amorphous (1200 nm), and solution (1150–2200 nm) states. Solution state: 1 mM in CH_2Cl_2. (B) 2PEF and 3PEF spectra of Au_4Ag_{13}–$SPhMe_2$ in crystalline (1300 nm), amorphous (1200 nm), and solution (1350 nm) states. Solution state: 1 mM in CH_2Cl_2. (C) Multiphoton linear fitting under optimal excitation of Au_4Ag_{13}–$SPhCl_2$ in crystalline (1300 nm), amorphous (1200 nm), and solution (1350 nm) states. (D) Multiphoton linear fitting under optimal excitation of Au_4Ag_{13}–$SPhMe_2$ in crystalline (1300 nm), amorphous (1200 nm), and solution (1350 nm) states. (E) 2PEF spectra of Au_4Ag_{13}–$SPhCl_2$ and Au_4Ag_{13}–$SPhMe_2$ in the amorphous state (1200 nm). (F) 2PA cross-section of Au_4Ag_{13}–$SPhCl_2$ and Au_4Ag_{13}–$SPhMe_2$ in the amorphous state (1200 nm). 1 GM = 10^{-50} cm^4 s^2 per photon per molecule. (G) 3PEF spectra of Au_4Ag_{13}–$SPhCl_2$ and Au_4Ag_{13}–$SPhMe_2$ in the crystalline state (1300 nm). (H) Optical limit response (1750 nm) of Au_4Ag_{13}–$SPhCl_2$ in the crystalline state. The black dots represent experimental data, and the red curve represents theoretical data. (I) Optical limit response (2150 nm) of Au_4Ag_{13}–$SPhCl_2$ in the crystalline state. The black dots represent experimental data, and the red curve represents theoretical data.

absorption (2PA) cross-section (δ) values of **Au_4Ag_{13}–SPhMe$_2$** were 937.60 GM under the 1450 nm excitation, almost the same as that of **Au_4Ag_{13}–SPhCl$_2$** (730.70 GM) under the 1250 nm excitation (Fig. 4F).

In the solution state, the intensity of the 2PEF spectra of **Au_4Ag_{13}–SPhMe$_2$** was higher than that of **Au_4Ag_{13}–SPhCl$_2$**, which was contradictory to the observation of PL characterization (Fig. 3C, D, 4A and B). Actually, such a mismatch was mainly reflected in the solution and the amorphous states. The reason might be the complex intermolecular interactions that can affect the excitation and emission pathways of such nanoclusters, while the tendencies for the cluster crystals were consistent (Fig. 4G). Significantly, the **Au_4Ag_{13}–SPhCl$_2$** cluster displayed apparent three-photon-excited fluorescence (3PEF) in its crystalline state, which was 3.6 times stronger than that of **Au_4Ag_{13}–SPhMe$_2$** (Fig. 4G, S17 and S18†). The NLO property of the **Au_4Ag_{13}–SPhCl$_2$** cluster in its crystalline state was investigated at 640 nm. The 3PEF spectra of **Au_4Ag_{13}–SPhCl$_2$** displayed a single emission peak, similar to its linear fluorescence spectra, except that the excitation wavelengths were roughly tripled. The introduction of the –Cl group afforded the D–A configured **Au_4Ag_{13}–SPhCl$_2$** with enhanced intramolecular charge transfer (ICT) behaviour and higher ΔE value (*i.e.*, HOMO–LUMO gap value), which would strengthen its multi-photon absorption activity (Fig. S12†).[56] In order to confirm the three-photon absorption (3PA) results, 3PA and excited state absorption (ESA) could be distinguished by measuring the intensity dependence of the nonlinear absorption coefficient γ.[57,58] For fs excitation, we obtained nearly constant γ values in the range of 10^{-21} cm^3 W^{-2} for clusters (Table S2†). In this context, a genuine multi-photon absorption (MPA) process, rather than a multi-step absorption process, was relevant for the nonlinearity shown in the fs excitation regime. It is worth underlining that this is the first report that the cluster crystals with precise structures can achieve 3PEF.[52]

Optical limiting is a nonlinear optical process in which the transmittance of a material decreases as the input light intensity increases.[59] Optical limiters can be exploited to fabricate devices for the protection of eyes and sensitive optical devices from laser-induced damage. The open aperture Z-scan results indicated the reverse saturable absorption (RSA) behaviour of nanoclusters, which was a clear manifestation of its optical

Open Access Article. Published on 26 July 2023. Downloaded on 5/4/2026 8:39:30 AM. This article is licensed under a Creative Commons Attribution-NonCommercial 3.0 Unported Licence.

limiting ability. Thus, the optical-limiting property of the clusters was investigated by a standard open aperture (OA) Z-scan technique (λ = 1750–2150 nm) by measuring the (energy-dependent) optical transmission at the focus (Fig. S19 and Table S3†).[60]

Fig. 4H and I show the transmitted energies of the **Au_4Ag_{13}–SPhCl$_2$** cluster as a function of the incident energy. At lower energy, the optical response obeys Beer's law very well. The transmitted energy started to deviate from the normal line and exhibited a typical limiting effect when the input energies reached about 0.040 and 0.051 J cm^{-2} under the corresponding excitations (1750 and 2150 nm). Accordingly, the transmitted energy started to deviate from the normal line and exhibited a typical limiting effect. The damaging thresholds were determined to be 0.171 and 0.176 J cm^{-2}. The damaging thresholds of **Au_4Ag_{13}–SPhCl$_2$** were determined to be 0.171 and 0.176 J cm^{-2}. The **Au_4Ag_{13}–SPhMe$_2$** cluster crystals also exhibited the optical-limiting effect (Fig. S20†), and the damaging thresholds were determined to be 0.177 and 0.178 J cm^{-2} under 1750 and 2150 nm excitations, respectively. In this context, the two cluster analogues were almost the same for the optical-limiting behaviour.

Besides, the open aperture Z-scan results indicated the reverse saturable absorption (RSA) behaviour of nanoclusters, which was a clear manifestation of its optical limiting ability. The optical limiting curves for **Au_4Ag_{13}–SPhCl$_2$** and **Au_4Ag_{13}–SPhMe$_2$** clusters in fs excitation regimes are presented in Fig. S21.† The optical limiting onset values were 0.0627 J cm^{-2} and 0.0749 J cm^{-2}, respectively, for **Au_4Ag_{13}–SPhCl$_2$** and **Au4Ag13–SPhMe2** nanoclusters under the 2150 nm fs-excitation (Table S4†), demonstrating that **Au_4Ag_{13}–SPhCl$_2$** was more likely to be applicable for optical limiting applications owing to its lower optical limiting onset value under the 2150 nm fs-excitation. However, under the 1750 nm fs-excitation, the optical limiting onset value of **Au_4Ag_{13}–SPhCl$_2$** was determined to be 0.0705 J cm^{-2}, much larger than that of the **Au_4Ag_{13}–SPhMe$_2$** cluster (0.0563 J cm^{-2}; Table S4†). Such a different optical limiting performance under different excitations is proposed to result from their different electronic structures. Indeed, owing to the ligand effect, the two Au_4Ag_{13} nanoclusters should display different geometric/electronic structures, and might exhibit distinct optical limiting tendencies under varying excitations. The optical limiting onset value for the reported $Au_9Ag_6(SPh^tOMe)_4(DPPOE)_3Cl_3$ nanocluster with excellent nonlinear optical properties was also determined for comparison (Fig. S21 and Table S4†).[61]

4 Conclusions

In summary, ligand engineering has been exploited to produce a new nanocluster, $Au_4Ag_{13}(DPPM)_3(SPhCl_2)_9$, bearing the intramolecular Ag···Cl interactions at the ligand shell–metallic kernel interface. Based on two Au_4Ag_{13} cluster analogues, the structure–property correlations have been investigated at the atomic level. We proved that the intra-cluster interactions in $Au_4Ag_{13}(DPPM)_3(SPhCl_2)_9$ remarkably restricted the intramolecular rotations, endowing this robust nanocluster with superior thermal stability, emission intensity, and non-linear optical properties over its cluster analogue, $Au_4Ag_{13}(DPPM)_3(SPhMe_2)_9$. Besides, $Au_4Ag_{13}(DPPM)_3(SPhCl_2)_9$ with enhanced properties has been successfully exploited as a new type of optical limiter. Overall, this work presents a novel case of the restriction of intramolecular rotation in the nanocluster field, which hopefully benefits the future design and preparation of new nanoclusters or cluster-based nanomaterials with customized structures and performances.

Data availability

The data that support the findings of this study are available in the ESI† of this article.

Author contributions

Junsheng Xin and Jing Xu carried out the experiments and analyzed the data. C. Z. and Y. T. assisted with the data analysis. Q. Z., X. K. and M. Z. designed the project, analyzed the data, and wrote the manuscript.

Conflicts of interest

There are no conflicts to declare.

Acknowledgements

We acknowledge the financial support of the NSFC (21631001, 21871001, and 22101001), the Ministry of Education, the University Synergy Innovation Program of Anhui Province (GXXT-2020-053), and the Scientific Research Program of Universities in Anhui Province (2022AH030009). Q. Z. acknowledges the financial support of the Nature Science Foundation of Anhui Province (2008085QB52).

Notes and references

1 R. Jin, C. Zeng, M. Zhou and Y. Chen, *Chem. Rev.*, 2016, **116**, 10346–10413.
2 I. Chakraborty and T. Pradeep, *Chem. Rev.*, 2017, **117**, 8208–8271.
3 X. Kang and M. Zhu, *Chem. Soc. Rev.*, 2019, **48**, 2422–2457.
4 X. Kang, Y. Li, M. Zhu and R. Jin, *Chem. Soc. Rev.*, 2020, **49**, 6443–6514.
5 M. Matus and H. Häkkinen, *Nat. Rev. Mater.*, 2023, **8**, 372–389.
6 W. Kurashige, Y. Niihori, S. Sharma and Y. Negishi, *Coord. Chem. Rev.*, 2016, **320**, 238–250.
7 H. Seong, Y. Jo, V. Efremov, Y. Kim, S. Park, S. M. Han, K. Chang, J. Park, W. Choi, W. Kim, C. H. Choi, J. S. Yoo and D. Lee, *J. Am. Chem. Soc.*, 2023, **145**, 2152–2160.
8 C. Zhu, J. Xin, J. Li, H. Li, X. Kang, Y. Pei and M. Zhu, *Angew. Chem., Int. Ed.*, 2022, **61**, e202205947.
9 A. Jana, M. Jash, W. A. Dar, J. Roy, P. Chakraborty, G. Paramasivam, S. Lebedkin, K. Kirakci, S. Manna, S. Antharjanam, J. Machacek, M. Kucerakova, S. Ghosh,

© 2023 The Author(s). Published by the Royal Society of Chemistry

Open Access Article. Published on 26 July 2023. Downloaded on 5/4/2026 8:39:30 AM. This article is licensed under a Creative Commons Attribution-NonCommercial 3.0 Unported Licence.

K. Lang, M. M. Kappes, T. Base and T. Pradeep, *Chem. Sci.*, 2023, **14**, 1613–1626.
10 M. Swierczewski, F. Cousin, E. Banach, A. Rosspeintner, L. M. L. Daku, A. Ziarati, R. Kazan, G. Jeschke, R. Azoulay, L.-T. Lee and T. Bürgi, *Angew. Chem., Int. Ed.*, 2023, **62**, e202215746.
11 T.-H. Chiu, J.-H. Liao, F. Gam, Y.-Y. Wu, X. Wang, S. Kahlal, J.-Y. Saillard and C. W. Liu, *J. Am. Chem. Soc.*, 2022, **144**, 10599–10607.
12 Y. Negishi, H. Horihata, A. Ebina, S. Miyajima, M. Nakamoto, A. Ikeda, T. Kawawaki and S. Hossain, *Chem. Sci.*, 2022, **13**, 5546–5556.
13 M. Agrachev, M. Ruzzi, A. Venzo and F. Maran, *Acc. Chem. Res.*, 2019, **52**, 44–52.
14 F. Fetzer, N. Pollard, N. C. Michenfelder, M. Strienz, A. N. Unterreiner, A. Z. Clayborne and A. Schnepf, *Angew. Chem., Int. Ed.*, 2022, **61**, e202206019.
15 W. W. Xu, X. Zeng and Y. Gao, *Acc. Chem. Res.*, 2018, **51**, 2739–2747.
16 Y.-J. Kong, J.-H. Hu, X.-Y. Dong, Y. Si, Z.-Y. Wang, X.-M. Luo, H.-R. Li, Z. Chen, S.-Q. Zang and T. C. W. Mak, *J. Am. Chem. Soc.*, 2022, **144**, 19739–19747.
17 S. Takano, S. Hasegawa, M. Suyama and T. Tsukuda, *Acc. Chem. Res.*, 2018, **51**, 3074–3083.
18 X. Liu, E. Wang, M. Zhou, Y. Wan, Y. Zhang, H. Liu, Y. Zhao, J. Li, Y. Gao and Y. Zhu, *Angew. Chem., Int. Ed.*, 2022, **61**, e202207685.
19 T.-A. D. Nguyen, Z. R. Jones, D. F. Leto, G. Wu, S. L. Scott and T. W. Hayton, *Chem. Mater.*, 2016, **28**, 8385–8390.
20 G. Deng, J. Kim, M. S. Bootharaju, F. Sun, K. Lee, Q. Tang, Y. J. Hwang and T. Hyeon, *J. Am. Chem. Soc.*, 2023, **145**, 3401–3407.
21 X. Ma, F. Sun, L. Qin, Y. Liu, X. Kang, L. Wang, D.-e. Jiang, Q. Tang and Z. Tang, *Chem. Sci.*, 2022, **13**, 10149–10158.
22 R.-W. Huang, Y.-S. Wei, X.-Y. Dong, X.-H. Wu, C.-X. Du, S.-Q. Zang and T. C. W. Mak, *Nat. Chem.*, 2017, **9**, 689–697.
23 Y. Zhu, L. Guo, J. Guo, L. Zhao, C. Li, X. Qiu, Y. Qin, X. Gu, X. Sun and Z. Tang, *Angew. Chem., Int. Ed.*, 2023, **62**, e202213208.
24 X. Kang, S. Wang, Y. Song, S. Jin, G. Sun, H. Yu and M. Zhu, *Angew. Chem., Int. Ed.*, 2016, **55**, 3611–3614.
25 G.-T. Xu, X.-Y. Chang, K.-H. Low, L.-L. Wu, Q. Wan, H.-X. Shu, W.-P. To, J.-S. Huang and C.-M. Che, *Angew. Chem., Int. Ed.*, 2022, **61**, e202200748.
26 J. Yan, B. K. Teo and N. Zheng, *Acc. Chem. Res.*, 2018, **51**, 3084–3093.
27 S.-S. Zhang, S. Havenridge, C. Zhang, Z. Wang, L. Feng, Z.-Y. Gao, C. M. Aikens, C.-H. Tung and D. Sun, *J. Am. Chem. Soc.*, 2022, **144**, 18305–18314.
28 B. Bhattarai, Y. Zaker, A. Atnagulov, B. Yoon, U. Landman and T. P. Bigioni, *Acc. Chem. Res.*, 2018, **51**, 3104–3113.
29 K. Yonesato, S. Yamazoe, S. Kikkawa, D. Yokogawa, K. Yamaguchi and K. Suzuki, *Chem. Sci.*, 2022, **13**, 5557–5561.
30 F. Hu, H.-W. Luyang, R.-L. He, Z.-J. Guan, Z.-J. Guan, S.-F. Yuan and Q.-M. Wang, *J. Am. Chem. Soc.*, 2022, **144**, 19365–19371.
31 M. Zhu, Q. Yao, Z. Liu, B. Zhang, Y. Lin, J. Liu, M. Long and J. Xie, *Angew. Chem., Int. Ed.*, 2022, **61**, e202115647.
32 W. Suzuki, R. Takahata, Y. Chiga, S. Kikkawa, S. Yamazoe, Y. Mizuhata, N. Tokitoh and T. Teranishi, *J. Am. Chem. Soc.*, 2022, **144**, 12310–12320.
33 Z.-R. Yuan, Z. Wang, B.-L. Han, C.-K. Zhang, S.-S. Zhang, Z.-Y. Zhu, J.-H. Yu, T.-D. Li, Y.-Z. Li, C.-H. Tung and D. Sun, *Angew. Chem., Int. Ed.*, 2022, **61**, e202211628.
34 X. Wei, K. Chu, J. R. Adsetts, H. Li, X. Kang, Z. Ding and M. Zhu, *J. Am. Chem. Soc.*, 2022, **144**, 20421–20433.
35 W. Fei, S. Antonello, T. Dainese, A. Dolmella, M. Lahtinen, K. Rissanen, A. Venzo and F. Maran, *J. Am. Chem. Soc.*, 2019, **141**, 16033–16045.
36 C. Hosier and C. J. Ackerson, *J. Am. Chem. Soc.*, 2019, **141**, 309–314.
37 Z. Luo, X. Yuan, Y. Yu, Q. Zhang, D. T. Leong, J. Y. Lee and J. Xie, *J. Am. Chem. Soc.*, 2012, **134**, 16662–16670.
38 Y. Jin, C. Zhang, X.-Y. Dong, S.-Q. Zang and T. C. W. Mak, *Chem. Soc. Rev.*, 2021, **50**, 2297–2319.
39 N. Goswami, Q. Yao, Z. Luo, J. Li, T. Chen and J. Xie, *J. Phys. Chem. Lett.*, 2016, **7**, 962–975.
40 D. Bera and N. Goswami, *J. Phys. Chem. Lett.*, 2021, **12**, 9033–9046.
41 X. Kang, S. Wang and M. Zhu, *Chem. Sci.*, 2018, **9**, 3062–3068.
42 P.-P. Sun, B.-L. Han, H.-G. Li, C.-K. Zhang, X. Xin, J.-M. Dou, Z.-Y. Gao and D. Sun, *Angew. Chem., Int. Ed.*, 2022, **61**, e202200180.
43 Y. Tian, S. Hu, X. Zhang, H. Gao, Y. Xiao, Y. Wang, D. Yao and H. Zhang, *Nano Res.*, 2023, **16**, 7733–7741.
44 Y. Zhang, Z. Lu, A. Feng, J. W. Y. Lam, Z. Wang, Y.-e. Shi and B. Z. Tang, *Chem.–Eur. J.*, 2023, **29**, e202203554.
45 H. Peng, Z. Huang, H. Deng, W. Wu, K. Huang, Z. Li, W. Chen and J. Liu, *Angew. Chem., Int. Ed.*, 2020, **59**, 9982–9985.
46 X. Pan, Z. Zuo, Z. Wang, G. Yang, H. Zhu, Y. Li and X. Yuan, *Mater. Chem. Front.*, 2023, **7**, 1146–1152.
47 S. Jin, W. Liu, D. Hu, X. Zou, X. Kang, W. Du, S. Chen, S. Wei, S. Wang and M. Zhu, *Chem.–Eur. J.*, 2018, **24**, 3712–3715.
48 M. Sugiuchi, J. Maeba, N. Okubo, M. Iwamura, K. Nozaki and K. Konishi, *J. Am. Chem. Soc.*, 2017, **139**, 17731–17734.
49 Z. Wu, H. Liu, T. Li, J. Liu, J. Yin, O. F. Mohammed, O. M. Bakr, Y. Liu, B. Yang and B. H. Zhang, *J. Am. Chem. Soc.*, 2017, **139**, 4318–4321.
50 Z. Xie, P. Sun, Z. Wang, H. Li, L. Yu, D. Sun, M. Chen, Y. Bi, X. Xin and J. Hao, *Angew. Chem., Int. Ed.*, 2020, **59**, 9922–9927.
51 X. Wei, X. Kang, S. Jin, S. Wang and M. Zhu, *CCS Chem.*, 2020, **2**, 1929–1939.
52 T. Chen, S. Yang, J. Chai, Y. Sing, J. Fan, B. Rao, H. Sheng, H. Yu and M. Zhu, *Sci. Adv.*, 2017, **3**, e1700956.
53 M. Walter, J. Akola, O. Lopez-Acevedo, P. D. Jadzinsky, G. Calero, C. J. Ackerson, R. L. Whetten, H. Grönbeck and H. Häkkinen, *Proc. Natl. Acad. Sci. U. S. A.*, 2008, **105**, 9157–9162.
54 X. Kang and M. Zhu, *Coord. Chem. Rev.*, 2019, **394**, 1–38.
55 Z. Wu and R. Jin, *Nano Lett.*, 2010, **10**, 2568–2573.

Open Access Article. Published on 26 July 2023. Downloaded on 5/4/2026 8:39:30 AM.
This article is licensed under a Creative Commons Attribution-NonCommercial 3.0 Unported Licence.

56 Z. H. Feng, D. D. Li, M. Z. Zhang, T. Shao, Y. Shen, X. H. Tian, Q. Zhang, S. L. Li, J. Y. Wu and Y. P. Tian, *Chem. Sci.*, 2019, **10**, 7228–7232.
57 B. Anand, A. Kaniyoor, S. S. S. Sai, R. Philip and S. Ramaprabhu, *J. Mater. Chem. C*, 2013, **1**, 2773–2780.
58 R. L. Sutherland, *Handbook of Nonlinear Optics*, 2003, ISBN: 0-8247-4243-5.
59 R. Philip, P. Chantharasupawong, H. Qian, R. Jin and J. Thomas, *Nano Lett.*, 2012, **12**, 4661–4667.
60 Q. Zhang, W.-L. Song, A. M. S. Hossain, Z.-D. Liu, G.-J. Hu, Y.-P. Tian, J.-Y. Wu, B.-K. Jin, H.-P. Zhou, J.-X. Yang and S.-Y. Zhang, *Dalton Trans.*, 2011, **40**, 3510–3516.
61 P. Y. Pan, L. L. Liu, L. D. Zhang, X. Wei, Y. P. Tian, X. Kang, Q. Zhang and M. Zhu, *Angew. Chem., Int. Ed.*, 2022, **61**, e202213016.

© 2023 The Author(s). Published by the Royal Society of Chemistry